Supplement of Biogeosciences, 21, 5653–5684, 2024
https://doi.org/10.5194/bg-21-5653-2024-supplement

Biogeosciences Open Access EGU

Supplement of

Were early Archean carbonate factories major carbon sinks on the juvenile Earth?

Wanli Xiang et al.

Correspondence to: Joachim Reitner (jreitne@gwdg.de)

S1. Necessary figures supporting the main text

Figure S1: Thin section photographs of interstitial carbonates and host basalts. (a–c) Decreasing sizes and density of carbonatized variolites in basaltic margin. (d) Breakup of the variolites resulting in anatase particles and calcite laths. (e) Secondary minerals include calcite, chlorite, anatase and epidote. (f–h) Migration of chlorite into interstitial space of basalt. (i) Schistose basalt cut by a calcite vein formed through brittle deformation. (a–f) are from the Apex Basalt, (g–i) from the Mount Ada Basalt. All photos were taken under plane-polarized light. Scale bar in (i) equals to 200 µm and applies to all photos. Abbreviations: Cal- calcite, An- anatase, Chl- chlorite, Qtz- quartz, Epi- epidote, Ank-ankerite.

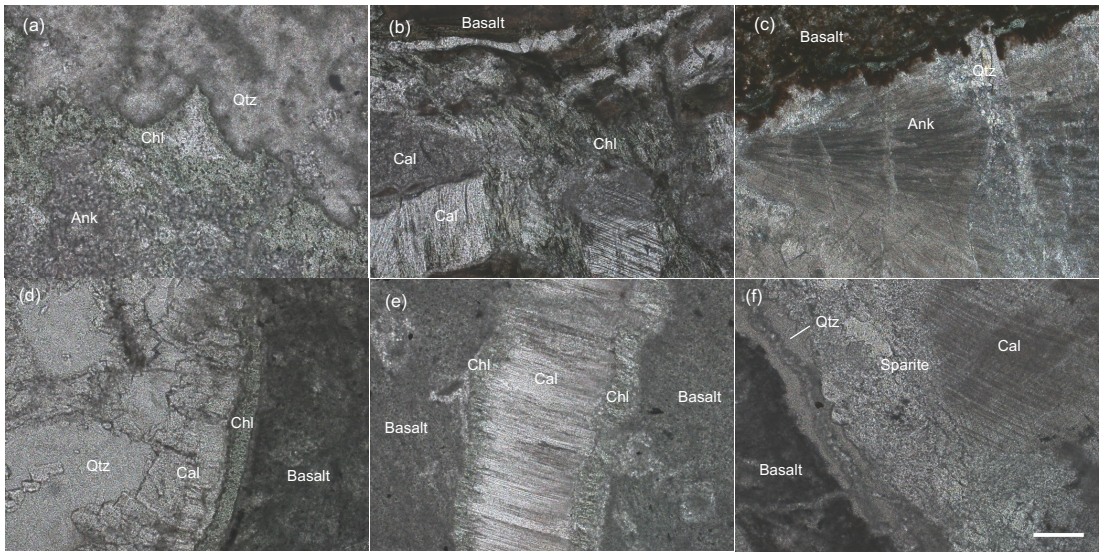

Figure S2: Thin section photographs showing the secondary carbonate facies of interstitial carbonates. (a) Microcrystalline ankerite (Ank) and quartz (Qtz) are rare and observed at the basalt margin, mixing with chlorite (Chl) and anatase particles (~nm). (b) Blocky calcite is the primary carbonate generation within concentric syngenetic veins in pillow basalt (near the cross A22-vein-2 in Fig. 3a). It was cemented by fibrous isopachous calcite during tectonic events. (c) A relict structure of acicular crystal-fan in ankerite. (d) Sharp contacts between edge of basalt, chlorite and isopachous calcite. (e) Contact in parallel veins within basalt, similar to those shown in (d). (f) Contacts of calcite in interspaces are distinct to those shown in (d), indicating that the studied calcite (D-2) formed within a wide fracture (therefore addressed as "fracture-filling calcite"). (a, b) are from Apex Basalt, (c) from Mount Ada Basalt, and (d–f) from the Dresser Formation. Photos were taken under plane-polarized light. The scale bar in (f) corresponds to 200 µm and applies to all photos.

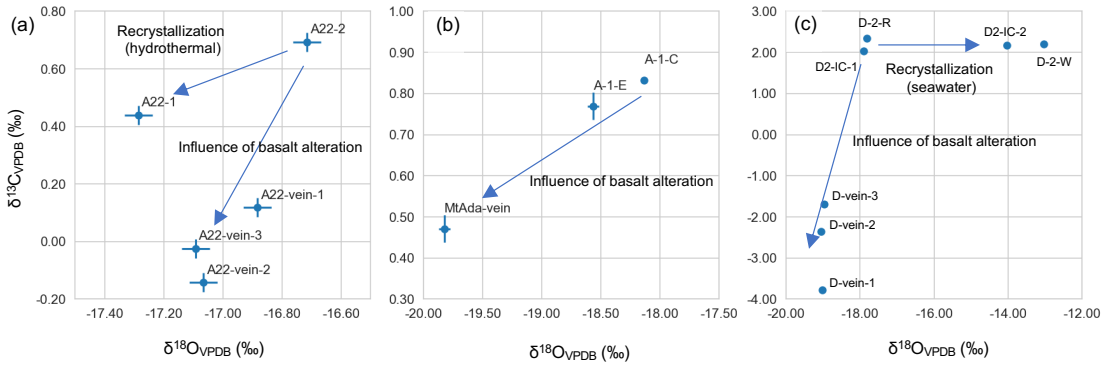

Figure S3: Cross-plots of $\delta^{13}C$ and $\delta^{18}O$ date for the interstitial carbonates and veinlet carbonates in samples (a) A22, (b) MtAda-1 and (c) D-2. The relative positions are marked in Figs. 3 and 5, respectively.

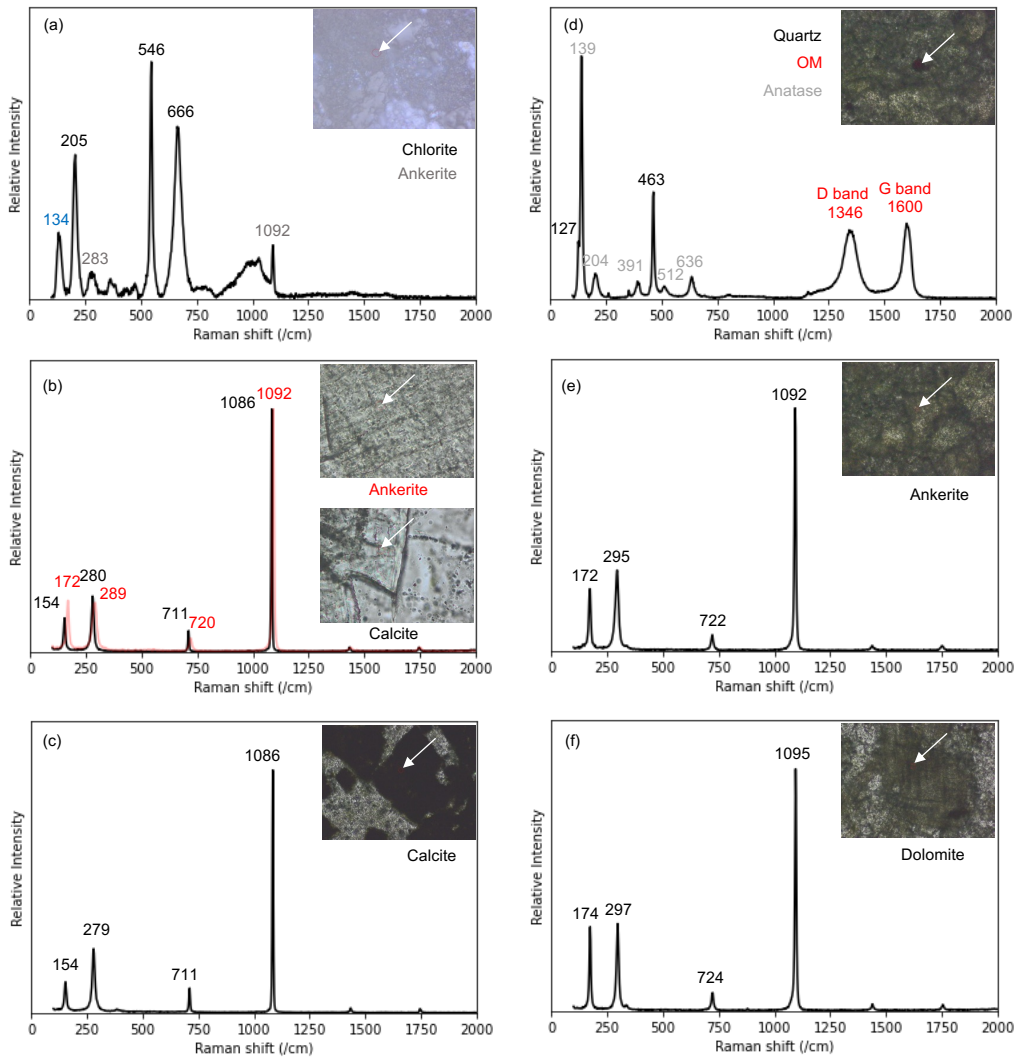

Figure S4: Raman spectra for mineral assemblages in the studied early Archean carbonates. (a) Minor ankerite mixing with chlorite at the margin of pillow basalt from the Apex Basalt. (b) Interstitial carbonates from the Mount Ada Basalt consist of ankerite overgrown by calcite. (c) Carbonate rhombs of the bedded carbonate from the Dresser Formation consist of calcite. (d) Anatase and quartz with encapsulated organic matter are interbedded with (e) ankerite of the bedded carbonate from the Euro Basalt. (f) Stromatolite of the Strelley Pool Formation mainly consist of dolomite.

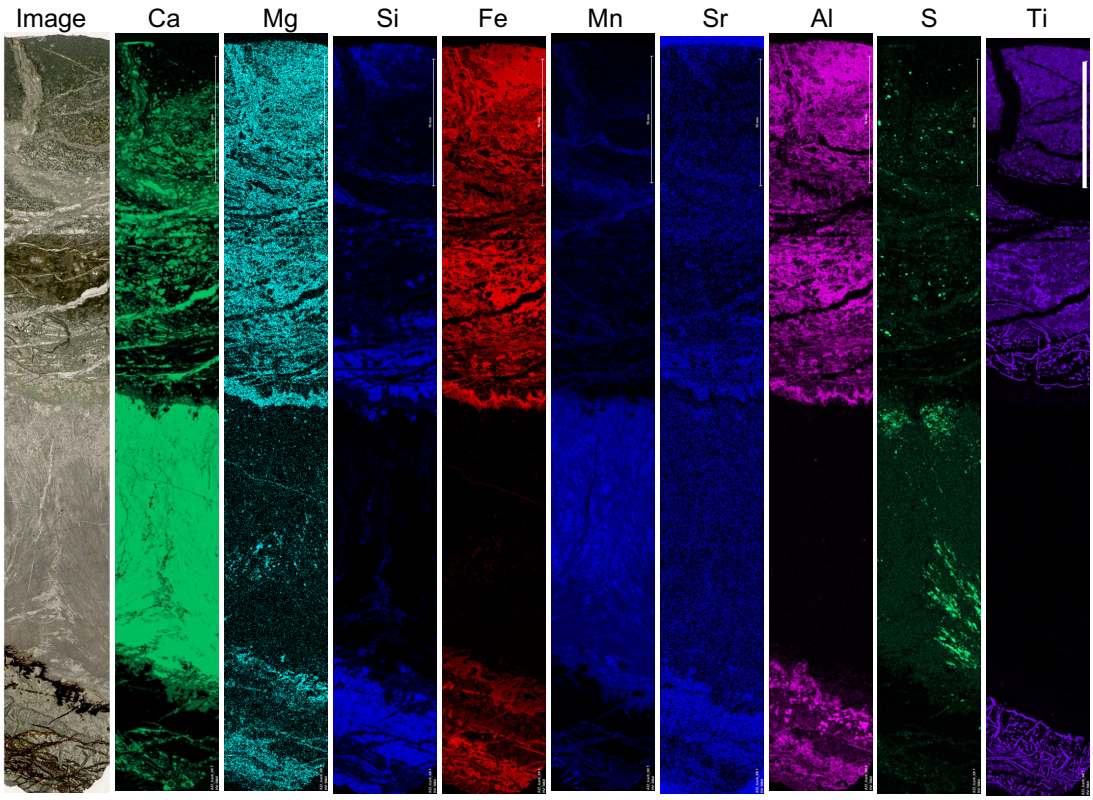

Figure S5: False-color element images of µXRF mappings, showing element distributions in interstitial carbonates from the Apex Basalt. The scale bar is 10 mm.

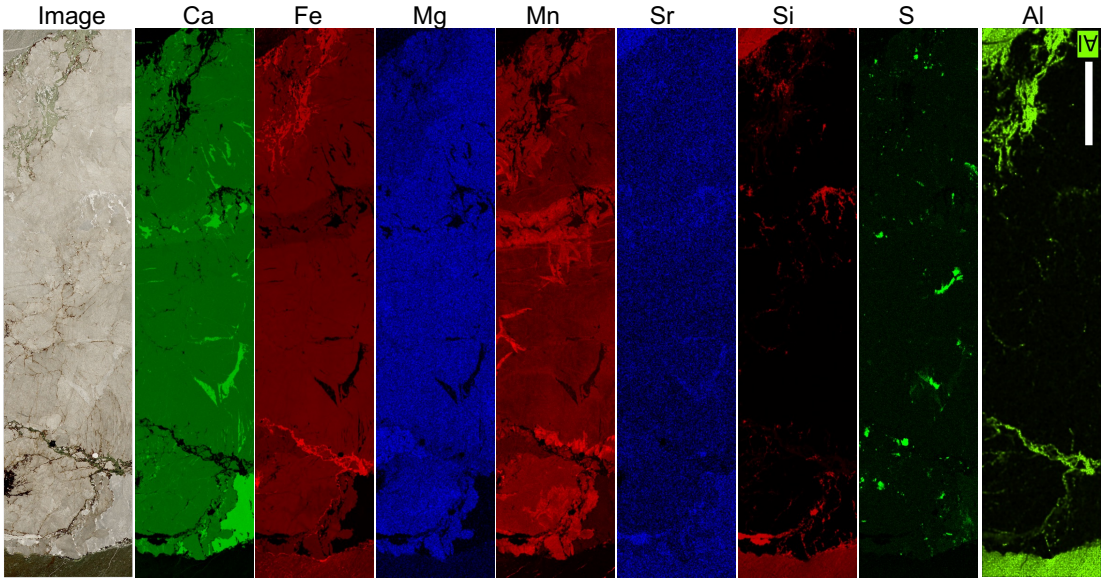

Figure S6: False-color element images of µXRF mappings, showing element distributions in interstitial carbonates from the Mount Ada Basalt. The scale bar is 10 mm.

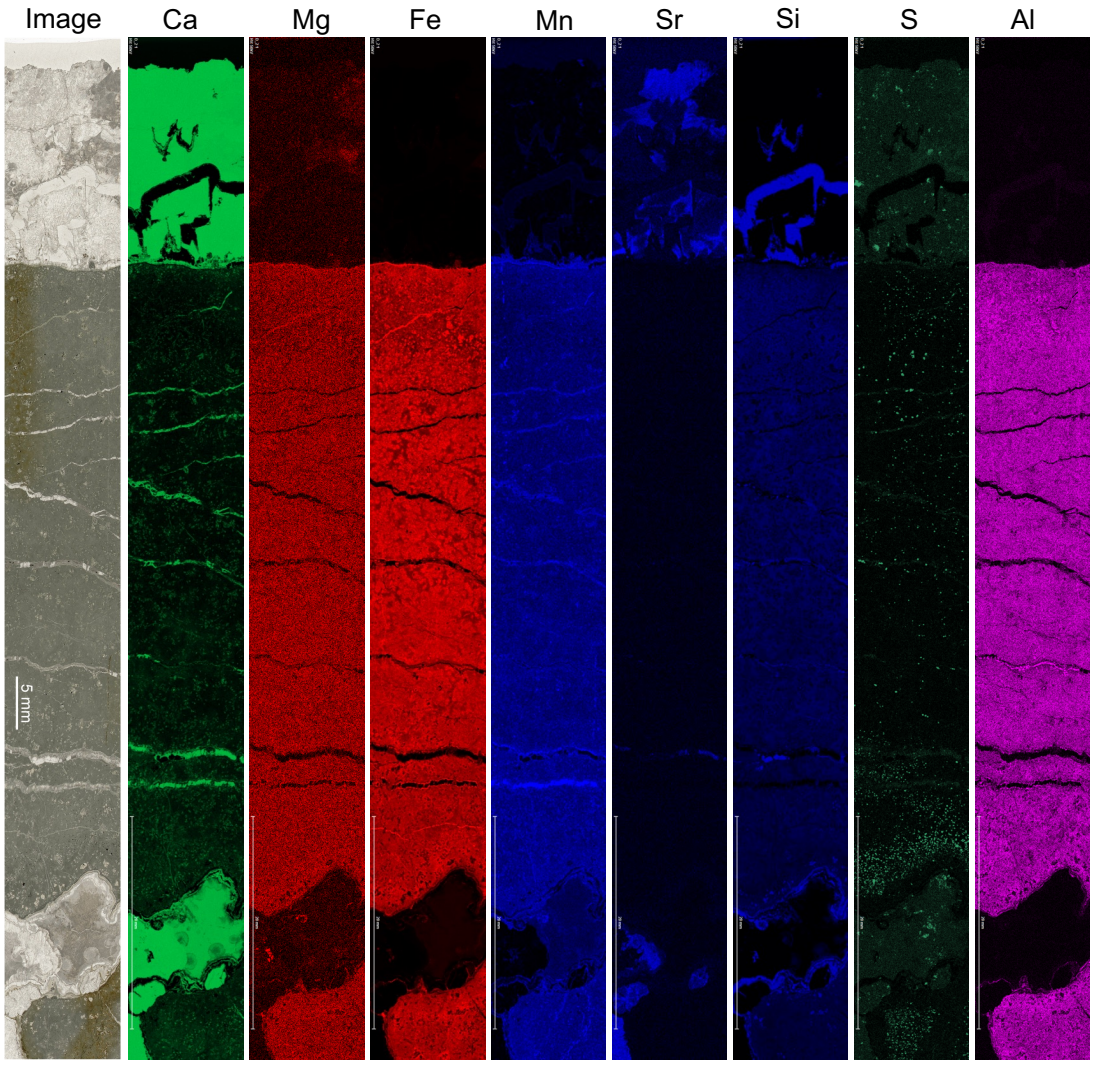

Figure S7: False-color element images of µXRF mappings, showing element distributions in interstitial carbonates from the Middle Basalt Member of Dresser Formation.

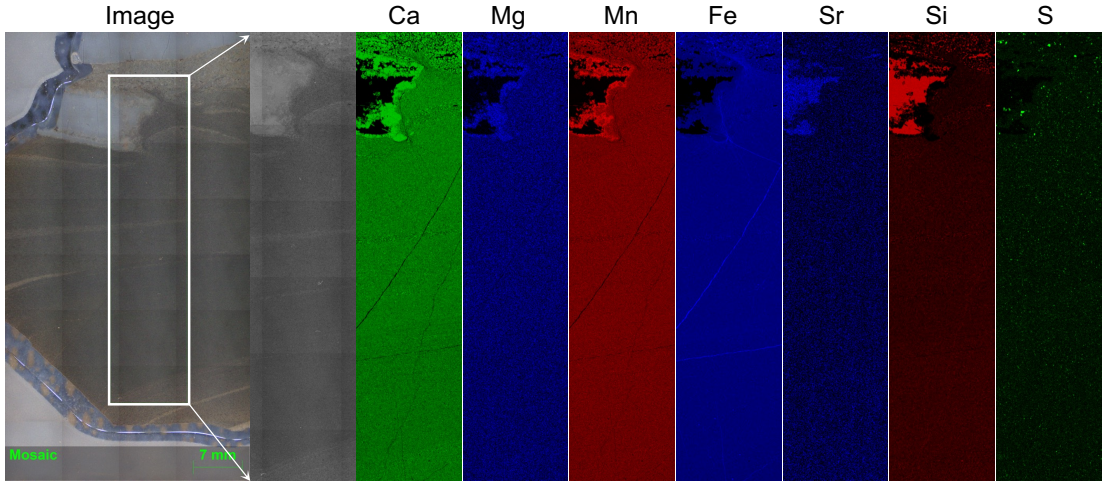

Figure S8: False-color element images of µXRF mappings, showing element distributions in the laminated micritic sedimentary carbonate of the Dresser Formation.

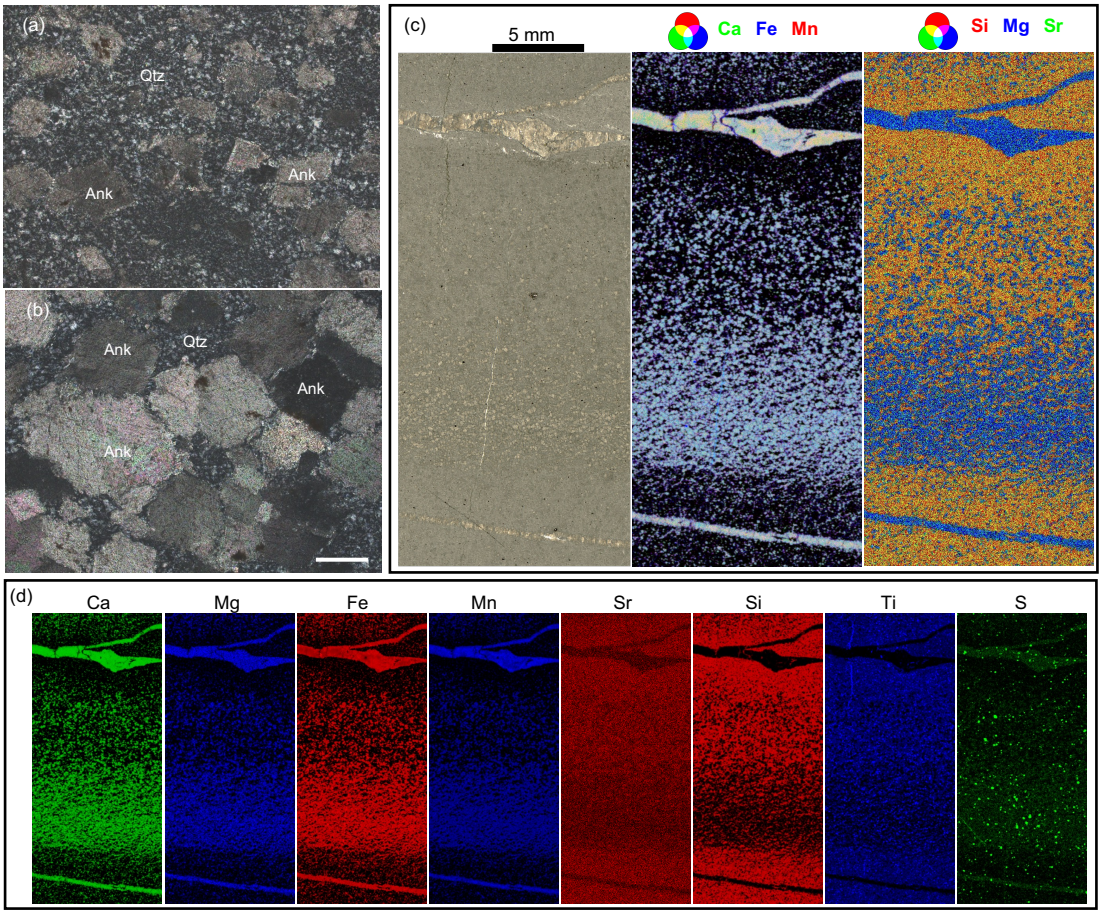

Figure S9: Images of the bedded sedimentary chert-carbonate from the Euro Basalt. (a) Subhedral to anhedral ankerite (Ank) rhombs in the microcrystalline quartz (Qtz) matrix in the upper part of a layer. (b) Ankerite rhombs are larger in the lower part of a layer, and experienced pressure dissolution. (c) False-color overlapping images show the size-grading of Fe- and Mn-enriched dolomite crystals and veins in a chert matrix. (d) False-color element images of µXRF mappings. (a) and (b) were taken under cross-polarized light; the scale bar corresponds to 200 µm.

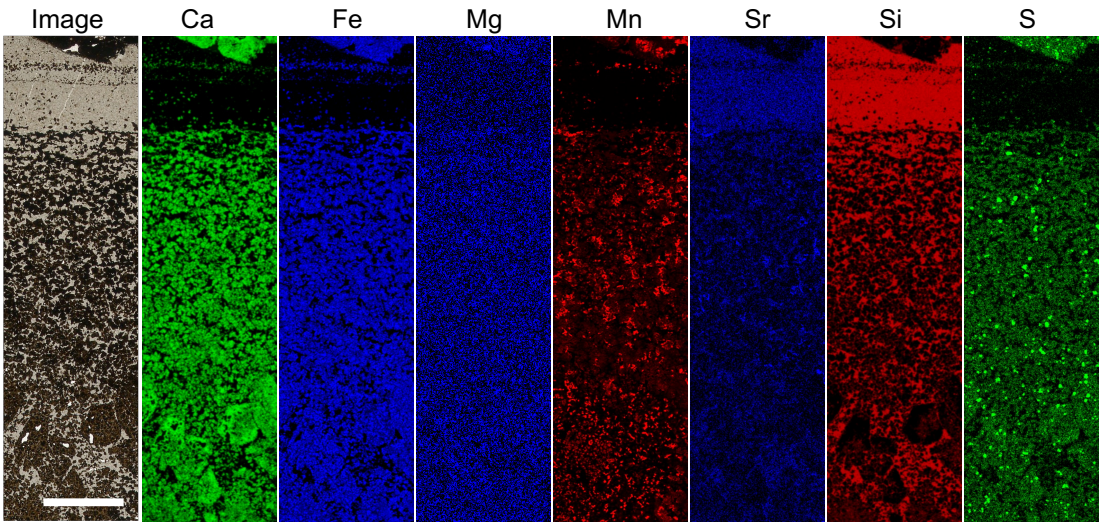

Figure S10: False-color element images of µXRF mappings, showing element distribution in the Dresser bedded carbonate. The scale bar is 5 mm.

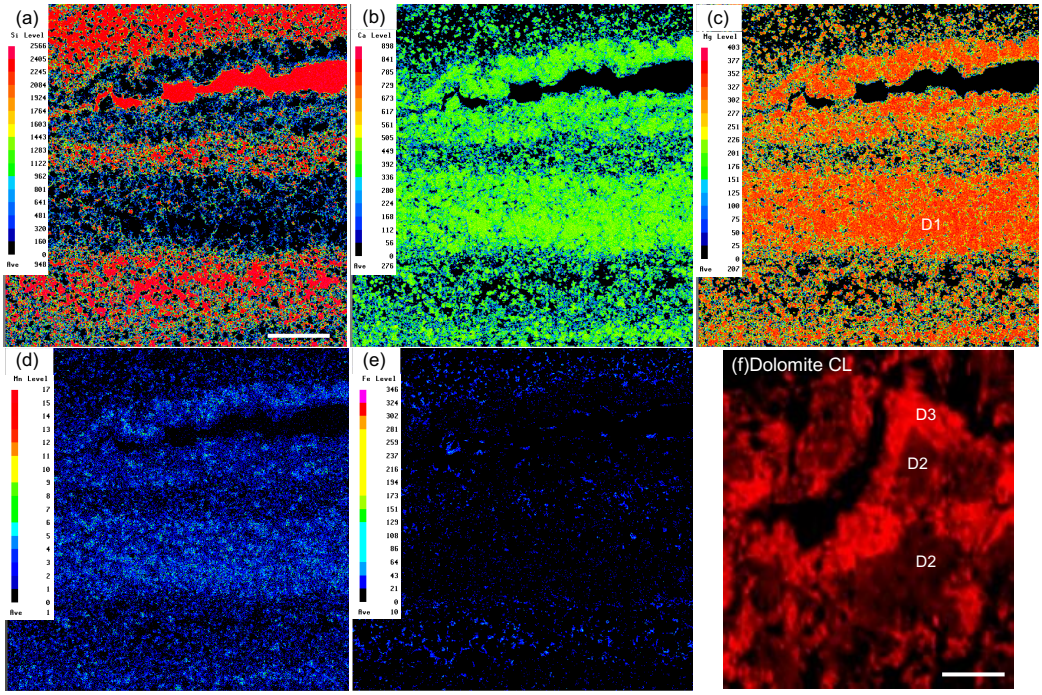

Figure S11: Images of the stromatolitic carbonates from the Strelley Pool Formation. EPMA mappings of (a) Si, (b) Ca, (c) Mg, (d) Mn, and (e) Fe, highlighting silicified laminae of Mn-enriched dolomites. (f) CL image of dolomite, illustrating the presence of a first generation (D1) followed by two recrystallized generations (D2 and D3). (a–e) EPMA analyses were conducted at 15 kV with a probe diameter of 10 µm using a JEOL 8900 RL electron microprobe instrument by Dr. Andreas Kronz (Department of Mineralogy, University of Göttingen). The scale bar in (a) corresponds to 2 mm and also applies to (b–e); the scale bar in (f) is 25 µm.

S2. Radiogenic Sr isotopic composition

The chips (diameter ~1 cm) of the primary interstitial carbonates (A22-2, ABAS-2, ABAS-3 and A14673-1 in Table 1; see Fig. S12), portions of the host basalts (core, margin and breccia; see Fig. S12), and the fracture filling calcites (D-2-W in Table 1), were drilled from sample sections, respectively.

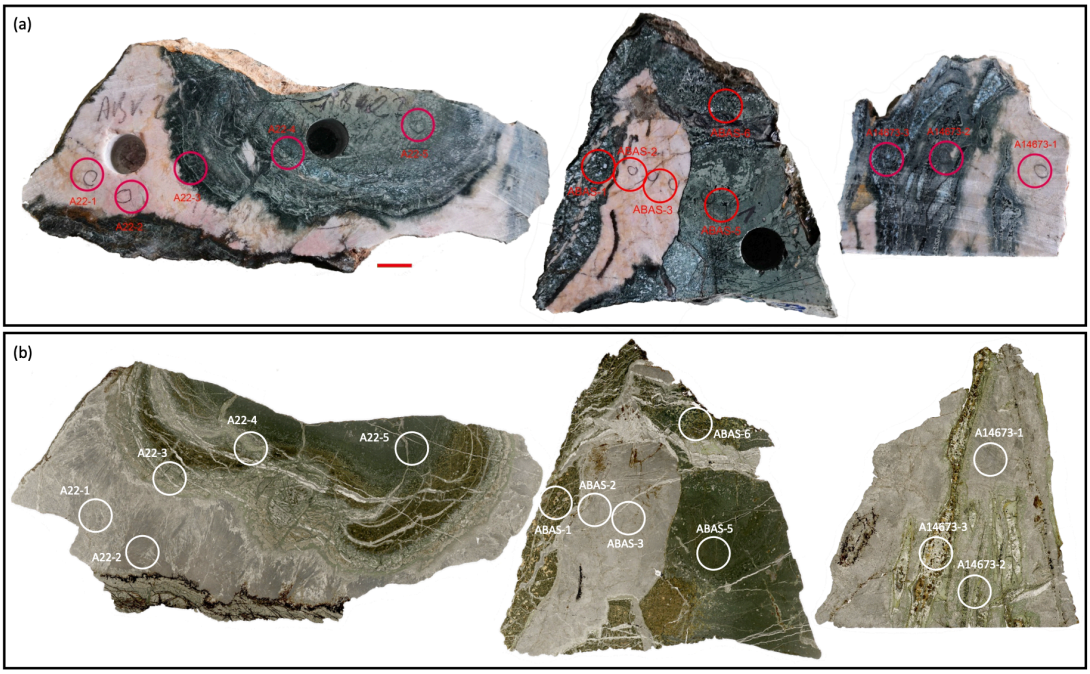

Figure S12: Photos of subsamples (columns of ca. 1 cm in diameter) drilled from (a) section A22, ABAS and A14673 (Scale bar: 1 cm). (b) Their lithologies are indicated on the relative thin sections (not completely matching; the scan images were taken under transmitted light).

A sequential leaching procedure was performed to dissolve carbonates (HNO_3, HCl, H_2O_2) and basalt (HNO_3, HCl, HF), avoiding contamination as much as possible (details see Xiang, 2023). Aliquots of sample solutions and reference materials Jls-1, Jdo-1 and JB-2 were spiked with ^{87}Rb-^{84}Sr tracer solutions and purified to collect Rb and Sr solutions using BioRad AG 50 × 8 (200–400 mesh) resin and Triskem Sr-spec Resin (50–100 μm), respectively.

The measurements were performed using a ThermoFisher Scientific Neptune Plus MC- ICPMS equipped with a Teledyne Cetac Aridus3 desolvation system to introduce sample solutions into the plasma. The $^{86}Sr/^{88}Sr$ ratio was normalized to 0.1194 using an exponential law. The determinations of $^{87}Sr/^{86}Sr$ ratios were obtained in static ion-collection mode, based on 100 mass scans for sample solutions and 40 scans for procedural blanks, respectively. Concentrations of Rb were determined using an ID-SF-ICPMS technique, as described in Willbold and Jochum (2005), on a ThermoFinnigan ELEMENT2 mass spectrometer. The current long-term, mean $^{87}Sr/^{86}Sr$ ratio of NIST SRM 987 is 0.710246 ± 0.000009 (2σ, n =48). The $^{87}Sr/^{86}Sr$ ratios of JDo-1, JLs-1 and JB-2 are 0.707575±28 (2σ, n=2), 0.707847±19 (2σ, n=2) and 0.703711 (n=1), respectively. All procedures and measurements were carried at the Geoscience center of Göttingen University.

The initial Sr isotopic compositions are calculated using the Rb decay constant λ of 1.397 ± 0.003 × $10^{-11}a^{-1}$ (Rotenberg et al., 2012), according to the following equation:

$$\left(\frac{^{87}Sr}{^{86}Sr}\right)_P = \left(\frac{^{87}Sr}{^{86}Sr}\right)_I + \frac{^{87}Rb}{^{86}Sr}\left(e^{\lambda t} - 1\right) \qquad \text{(Eq. S1)}$$

where $(^{87}Sr/^{86}Sr)_p$ is present-day Sr isotope ratio that is measured by mass spectrometry, and $(^{87}Sr/^{86}Sr)_I$ is the initial Sr isotope ratio. The Rb-Sr system of basalts can be used in geochronology by plotting $^{87}Sr/^{86}Sr$ (y axis) against $^{87}Rb/^{86}Sr$ (x axis), yielding a linear regression line whose intercept is the initial $(^{87}Sr/^{86}Sr)_I$ of the rock system, and slope ($e^{\lambda t} - 1$) is used to calculate the age. The geochronology is achieved via IsoplotR (Vermeesch, 2018).

The Rb–Sr isochron based on all Apex pillow basalts (n=8) yields an age of 3695.3 ± 231.1 Ma and an initial $^{87}Sr/^{86}Sr$ ratio of 0.705198 ± 0.001327 with mean squared weighted deviates (MSWD) of 440 (Fig. S13a), implying the age is over-dispersed with respect to the stated analytical uncertainties. After excluding two highly carbonatized samples (A14673-3 and ABAS-1), the 6-points Rb–Sr isochron yields an age of 3570.7 ± 144.3 Ma and an initial $^{87}Sr/^{86}Sr$ ratio of 0.706337 ± 0.000954 with MSWD= 150 (Fig. S13b). The large MSWD value illustrates that it is an errorchron instead of an isochron. Nonetheless, the errorchron age is comparable to the depositional age of Apex Basalt, implying that the Rb-Sr system of the studied Apex basalt has not been reset during oceanic crust carbonatization. The carbonatization was syn-depositional or occurred soon after the eruption of pillow lava.

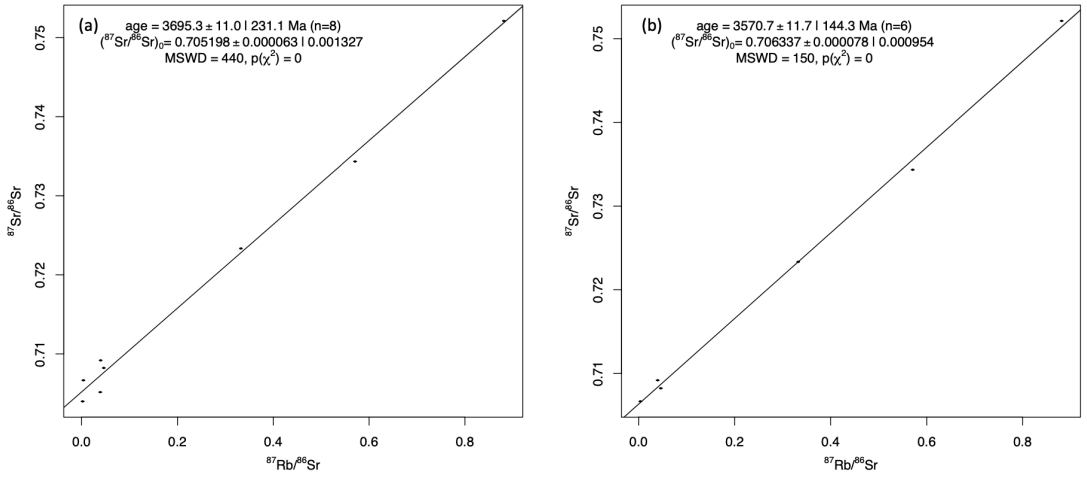

Figure S13: The Rb–Sr whole-rock isochron diagram for Apex pillow basalts, produced using IsoplotR (Vermeesch, 2018). (a) The large MSWD indicates the 8-point isochron is an errorchron. (b) After excluding two highly carbonatized subsamples, a 6-point errorchron yields an age of metamorphism identical to the depositional age of the Apex Basalt (ca. 3460 Ma).

The $^{87}Sr/^{86}Sr(i)$ ratios (after correction of Rb and age) were shown in Table S1, including values for fracture-filling calcite D-2-W, the primary interstitial calcites and their respective host pillowed basalts. Notably, the fracture-filling calcite exhibits the lowest $^{87}Sr/^{86}Sr(i)$ ratio (0.700596), close to the lowest reported ratios for barites from the same geological formation (0.700502 in McCulloch, 1994; 0.700447 in Chen et al., 2022). This congruence suggests a likely origin from seawater carbonate precipitation.

The primary interstitial calcites display $^{87}Sr/^{86}Sr(i)$ ratios spanning from 0.701796 to 0.704172, with a mean of 0.706337 ± 0.000954. These values are positioned between those representative values of the early Archean seawater (0.700596) and altered oceanic crust (0.706337 ± 0.000954), suggesting precipitation from fluids resulting from the interaction between seawater and oceanic crust during the early Archean era.

Table S1: The $^{87}Sr/^{86}Sr(i)$ ratios of one fracture-filling calcite, primary interstitial calcites and their respective host pillowed basalts.

Sorts	Mineralogy	Formation	Age (Ma)	Sample ID	$^{87}Sr/^{86}Sr(i)$	$^{87}Sr/^{86}Sr(i)$*
Apex pillow basalt	Calcite + chlorite + anatase + quartz ± pyrite	Apex Basalt	3460	A14673-2	0.706483	0.706337 ± 0.000954 [a]
				A14673-3	0.703894	
				A22-3	0.706605	
				A22-4	0.707188	
				A22-5	0.707742	
				ABAS-1	0.703207	
				ABAS-5	0.705601	
				ABAS-6	0.705904	
Primary interstitial carbonate	Calcite			A14673-1	0.703159	0.703094 ± 0.000979 [b]
				A22-2	0.704172	
				ABAS-2	0.703250	
				ABAS-3	0.701796	
Fracture-filling calcite		Dresser Formation	3480	D-2-W	0.700596	

Note:

1. $^{86}Sr/^{88}Sr$ ratio was normalized to 0.1194 using an exponential law.

2. $^{87}Sr/^{86}Sr$ ratio of NIST SRM 987 is 0.710246 ± 0.000009 (2σ, n =48).

3. $^{87}Sr/^{86}Sr$ ratios of references JDo-1, JLs-1 and JB-2 are 0.707575 ± 28 (2σ, n=2), 0.707847±19 (2σ, n=2) and 0.703711 (n=1), respectively.

4. $^{87}Sr/^{86}Sr(i)$ are $^{87}Sr/^{86}Sr$ ratios after correction of Rb and age.

5. Values in $^{87}Sr/^{86}Sr(i)$* are the whole-rock $^{87}Sr/^{86}Sr$ ratio (superscript [a]) of the Apex pillow basalts yielded by the errorchron in Fig. S13 and the average $^{87}Sr/^{86}Sr$ ratio of the primary interstitial carbonates (superscript [b]), respectively.

S3. Ca and Si mass changes during basalt carbonatization

In-situ geochemical analysis of non-carbonate facies within pillowed basalt thin sections was performed, focusing on an area adjacent to A22-vein-3, extending from the basalt margin to its core (see Fig. 3a). This analysis was accomplished through the acquisition of point spectra utilizing a Bruker M4 Tornado micro-X-ray fluorescence instrument, equipped with an advanced XFlash 430 Silicon Drift Detector, enabling precise compositional characterization. Measurements were performed at 50 kV voltage and 200 μA, with a spot size of 20 μm and a chamber pressure of 20 mbar. All procedures and measurements were carried at the Geoscience center of Göttingen University.

In order to quantify the actual element gains and losses, relative chemical changes have been extensively adopted based on mass balance of an immobile element during metamorphism (Brimhall and Dietrich, 1987; MacLean and Barrett, 1993; Ague, 2017; Caruso et al., 2021). Considering that the EPT basaltic rocks have undergone regional metamorphism of up to greenschist facies (Nakamura and Kato, 2004; Smithies et al., 2005; Van Kranendonk et al., 2002, 2019) and the magma source of Apex basalt is derived from mantle plumes (Smithies et al., 2005; Van Kranendonk et al., 2007, 2015, 2019; Barnes and Arndt, 2019; Hasenstab et al., 2021; Tusch et al., 2021), which approaches compositions of Primitive Mantle (PM, Condie, 2005), the element concentrations of the PM are used for reference (after Palme and O'Neil, 2014). Zr is utilized as the reference element due to its largely immobility during hydrothermal alteration (Finlow–Bates and Stumpfl, 1981; MacLean and Kranidiotis, 1987; Ague, 2017). The total change in rock mass Δm_i^{rm} and the fractional change Δm_i^j of element j on the basis of reference (immobile) element *i* can be calculated as follows:

$$\Delta m_i^{rm} = \left(\frac{C_i^P}{C_i^A}\right) - 1 \qquad \text{(Eq. S2)}$$

$$\Delta m_i^j = \left(\frac{C_i^P}{C_i^A}\right)\left(\frac{C_j^A}{C_j^P}\right) - 1 \qquad \text{(Eq. S3)}$$

where *C* with subscripts *i* and *j* are concentrations of reference element *i* and element of interest *j*, and the ^{P} and ^{A} superscripts refer to the pristine and altered states, respectively. Percentage change is obtained by multiplying by 100 to reflect element gain or loss during alteration (gain is positive, loss negative). The concentrations of Ca, Si and Zr of PM are 2.61 wt%, 21.22 wt% and 10.3 ppm, respectively (after Palme and O'Neil, 2014).

The variations in the mass of Si and Ca relative to their positions within the basaltic matrix are graphically depicted in Figure S14, with quantitative outcomes summarized in Table S2. The negative Si mass changes observed in variolitic and spherulitic zones signify a net loss of Si in the altered zone. Conversely, positive Si values at the basalt margin attest to a Si gain. Notably, the mass changes of Ca exhibit positivity within the variolitic zone, indicating a gain of Ca therein, whereas other zones experience a loss. To be noted, the values calculated in this way can only qualitatively indicate the gain or loss of Si and Ca due to uncertainties in the measurements (without standards and reference materials for reproducibility and quality control).

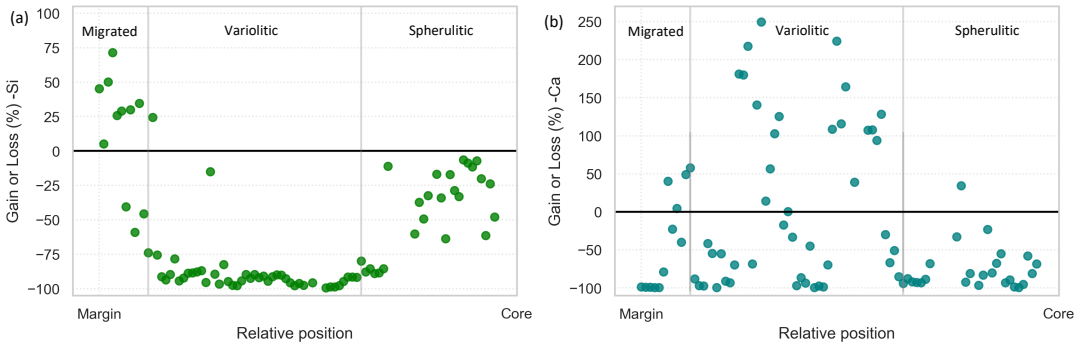

Figure S14: Mass changes of (a) Si and (b) Ca from margin to core in Apex pillow basalt A22 (Fig.3a). Data were only calculated with point spectra of non-carbonate facies via micro-XRF.

Nonetheless, these findings align with elemental mapping data presented in Figure 3b, reinforcing the notion that during oceanic crust carbonatization, the core and spherulitic zones of the pillow basalt undergo Ca depletion, whereas the variolitic zone undergoes a more intensified carbonatization process. The average Ca mass loss, quantified as -22.57%, indicates a substantial 22.57% reduction in Ca during oceanic crust carbonization. This value is subsequently employed in Eq. 6 of the main text to estimate the carbon flux sequestered within the oceanic crust factory.

Table S2: The concentrations of Zr (ppm), Si and Ca (wt%) acquired from point spectra of micro-XRF, and mass gain-loss of Ca and Si (%).

		Concentration			Gain or Loss	
SampleID	**Position***	**Zr (ppm)**	**Si (wt%)**	**Ca (wt%)**	**Si (%)**	**Ca (%)**
A22_blt_line_ 006	6	10.87	32.52	0.03	45.24	-98.73
A22_blt_line_ 007	7	14.82	32.11	0.03	5.18	-99.10
A22_blt_line_ 008	8	10.55	32.64	0.02	50.13	-99.19
A22_blt_line_ 009	9	9.21	32.55	0.02	71.46	-99.25
A22_blt_line_ 010	10	12.54	32.52	0.03	25.88	-99.21
A22_blt_line_ 011	11	11.43	30.37	0.61	28.94	-78.88
A22_blt_line_ 012	12	20.56	25.20	7.31	-40.50	40.40
A22_blt_line_ 013	13	11.41	30.58	2.23	30.07	-22.83
A22_blt_line_ 014	14	25.75	21.70	6.82	-59.10	4.44
A22_blt_line_ 015	15	10.96	30.39	1.67	34.65	-39.68
A22_blt_line_ 016	16	22.06	24.70	8.32	-45.66	48.88
A22_blt_line_ 017	17	30.89	16.62	12.34	-73.89	57.71
A22_blt_line_ 018	18	11.90	30.50	0.36	24.45	-87.95
A22_blt_line_ 019	19	32.64	16.40	0.24	-75.62	-97.10
A22_blt_line_ 020	20	54.07	9.74	0.38	-91.26	-97.19
A22_blt_line_ 021	21	58.21	7.56	8.60	-93.70	-41.67
A22_blt_line_ 022	22	44.28	9.40	5.09	-89.70	-54.65
A22_blt_line_ 023	23	37.15	16.62	0.04	-78.28	-99.57
A22_blt_line_ 024	24	95.18	11.09	10.87	-94.34	-54.91

A22_blt_line_ 025	25	56.45	9.07	1.25	-92.20	-91.23
A22_blt_line_ 026	26	43.99	10.14	0.77	-88.81	-93.05
A22_blt_line_ 027	27	46.26	10.98	3.58	-88.48	-69.46
A22_blt_line_ 028	28	40.37	10.21	28.77	-87.72	181.24
A22_blt_line_ 029	29	40.06	10.85	28.44	-86.85	180.11
A22_blt_line_ 030	30	47.70	4.42	38.38	-95.50	217.54
A22_blt_line_ 031	31	16.12	28.25	1.29	-14.92	-68.45
A22_blt_line_ 032	32	44.08	9.60	26.87	-89.43	140.54
A22_blt_line_ 033	33	46.65	3.20	41.32	-96.67	249.59
A22_blt_line_ 034	34	40.30	14.57	11.69	-82.45	14.44
A22_blt_line_ 035	35	54.68	5.98	21.73	-94.69	56.81
A22_blt_line_ 036	36	64.67	3.28	33.20	-97.54	102.59
A22_blt_line_ 037	37	58.25	2.68	33.24	-97.77	125.20
A22_blt_line_ 038	38	58.36	6.80	12.26	-94.34	-17.06
A22_blt_line_ 039	39	56.08	12.03	14.27	-89.59	0.41
A22_blt_line_ 040	40	50.12	7.89	8.50	-92.36	-33.08
A22_blt_line_ 041	41	46.70	10.05	0.35	-89.55	-97.06
A22_blt_line_ 042	42	55.12	9.19	1.88	-91.91	-86.56
A22_blt_line_ 043	43	53.13	9.98	0.88	-90.88	-93.45
A22_blt_line_ 044	44	60.35	6.80	8.44	-94.53	-44.79
A22_blt_line_ 045	45	53.44	9.64	0.05	-91.24	-99.61
A22_blt_line_ 046	46	49.58	10.24	0.35	-89.97	-97.25
A22_blt_line_ 047	47	50.98	10.31	0.18	-90.19	-98.64
A22_blt_line_ 048	48	55.58	8.39	4.30	-92.68	-69.44
A22_blt_line_ 049	49	46.10	4.07	24.38	-95.71	108.67
A22_blt_line_ 050	50	50.72	2.27	41.69	-97.83	224.35
A22_blt_line_ 051	51	50.73	4.03	27.75	-96.14	115.85
A22_blt_line_ 052	52	58.07	3.04	38.90	-97.46	164.34
A22_blt_line_ 054	54	56.11	5.06	19.77	-95.62	39.07
A22_blt_line_ 057	57	80.55	0.97	42.31	-99.41	107.31
A22_blt_line_ 058	58	73.26	1.86	38.55	-98.77	107.66
A22_blt_line_ 059	59	65.05	1.89	31.98	-98.59	93.98
A22_blt_line_ 061	60	63.16	3.00	36.52	-97.70	128.17
A22_blt_line_ 063	61	63.16	6.93	11.26	-94.68	-29.62
A22_blt_line_ 064	62	50.59	8.79	4.29	-91.57	-66.50
A22_blt_line_ 065	63	50.19	8.80	6.24	-91.49	-50.90
A22_blt_line_ 066	64	61.89	10.46	2.33	-91.80	-85.16
A22_blt_line_ 067	65	38.59	15.99	0.57	-79.89	-94.13
A22_blt_line_ 068	66	45.65	11.42	1.41	-87.86	-87.83
A22_blt_line_ 069	67	46.60	13.84	0.95	-85.58	-91.92
A22_blt_line_ 070	68	47.71	10.85	0.88	-88.96	-92.71
A22_blt_line_ 071	69	41.25	9.75	0.74	-88.53	-92.95
A22_blt_line_ 072	70	43.74	13.15	1.28	-85.41	-88.49
A22_blt_line_ 073	71	15.30	28.05	1.24	-11.02	-67.89

A22_blt_line_ 079	77	28.26	23.17	4.80	-60.20	-32.93
A22_blt_line_ 080	78	19.97	25.85	6.80	-37.19	34.30
A22_blt_line_ 081	79	22.66	23.67	0.45	-49.31	-92.09
A22_blt_line_ 082	80	19.68	27.39	0.94	-32.42	-81.15
A22_blt_line_ 084	82	17.09	29.31	0.15	-16.75	-96.55
A22_blt_line_ 085	83	19.96	27.17	0.86	-33.93	-82.96
A22_blt_line_ 086	84	27.79	20.84	5.41	-63.60	-23.23
A22_blt_line_ 087	85	16.81	28.74	0.85	-17.03	-80.16
A22_blt_line_ 088	86	18.76	27.52	1.55	-28.79	-67.45
A22_blt_line_ 089	87	19.54	26.98	2.23	-33.01	-55.00
A22_blt_line_ 090	88	15.35	29.62	0.26	-6.36	-93.23
A22_blt_line_ 091	89	15.80	29.67	0.42	-8.81	-89.45
A22_blt_line_ 092	90	15.99	29.18	0.06	-11.42	-98.60
A22_blt_line_ 093	91	15.56	29.81	0.03	-7.04	-99.23
A22_blt_line_ 094	92	16.32	26.83	0.20	-20.21	-95.11
A22_blt_line_ 095	93	28.16	22.42	3.01	-61.35	-57.86
A22_blt_line_ 096	94	17.03	26.74	0.83	-23.82	-80.79
A22_blt_line_ 097	95	21.67	23.29	1.73	-47.81	-68.50
Average Value					-60.24	-22.57

*** The increases of the numbers in Sample ID reflect approaching to the basalt core.**

Reference

Ague, J. J.: Element mobility during regional metamorphism in crustal and subduction zone environments with a focus on the rare earth elements (REE), American Mineralogist: Journal of Earth and Planetary Materials, 102, 1796–1821, https://doi.org/10.2138/am-2017-6130, 2017.

Barnes, S. and Arndt, N.: Distribution and geochemistry of komatiites and basalts through the Archean, in: Earth's Oldest Rocks, edited by Van Kranendonk, M., Bennett, V., and Hoffmann, J., 103–132, Elsevier, Amsterdam, https://doi.org/10.1016/B978-0-444-63901-1.00006-X, 2019.

Brimhall, G. H. and Dietrich, W. E.: Constitutive mass balance relations between chemical composition, volume, density, porosity, and strain in metasomatic hydrochemical systems: results on weathering and pedogenesis, Geochimica et Cosmochimica Acta, 51, 567–587, https://doi.org/10.1016/0016-7037(87)90070-6, 1987.

Caruso, S., Van Kranendonk, M. J., Baumgartner, R. J., Fiorentini, M. L., and Forster, M. A.: The role of magmatic fluids in the ~3.48 Ga Dresser Caldera, Pilbara Craton: New insights from the geochemical investigation of hydrothermal alteration, Precambrian Research, 362, 106 299, https://doi.org/10.1016/j.precamres.2021.106299, 2021.

Chen, X., Zhou, Y., and Shields, G. A.: Progress towards an improved Precambrian seawater 87Sr/86Sr curve, Earth-Science Reviews, 224, 103 869, https://doi.org/10.1016/j.earscirev.2021.103869, 2022.

Condie, K. C.: High field strength element ratios in Archean basalts: a window to evolving sources of mantle plumes?, Lithos, 79, 491–504, https://doi.org/10.1016/j.lithos.2004.09.014, 2005.

Finlow-Bates, T. and Stumpfl, E. F.: The behaviour of so-called immobile elements in hydrothermally altered rocks associated with volcanogenic submarine-exhalative ore deposits, Mineralium Deposita, 16, 319–328, https://doi.org/10.1007/BF00202743, 1981.

Hasenstab, E., Tusch, J., Schnabel, C., Marien, C., Van Kranendonk, M., Smithies, H., Howard, H., Maier, W., and Münker, C.: Evolution of the early to late Archean mantle from Hf-Nd-Ce isotope systematics in basalts and komatiites from the Pilbara Craton, Earth and Planetary Science Letters, 553, 116 627, https://doi.org/10.1016/j.epsl.2020.116627, 2021.

MacLean, W. and Kranidiotis, P.: Immobile elements as monitors of mass transfer in hydrothermal alteration; Phelps Dodge massive sulfide deposit, Matagami, Quebec, Economic Geology, 82, 951–962, https://doi.org/10.2113/gsecongeo.82.4.951, 1987.

MacLean, W. and Barrett, T.: Lithogeochemical techniques using immobile elements, Journal of geochemical exploration, 48, 109–133, https://doi.org/10.1016/0375-6742(93)90002-4, 1993.

McCulloch, M. T.: Primitive $^{87}Sr/^{86}Sr$ from an Archean barite and conjecture on the Earth's age and origin, Earth and planetary science letters, 126, 1–13, https://doi.org/10.1016/0012-821X(94)90238-0, 1994.

Nakamura, K. and Kato, Y.: Carbonatization of oceanic crust by the seafloor hydrothermal activity and its significance as a CO_2 sink in the Early Archean, Geochimica et Cosmochimica Acta, 68, 4595–4618, https://doi.org/10.1016/j.gca.2004.05.023, 2004.

Palme, H. and O'Neill, H.: 3.1 Cosmochemical estimates of mantle composition, in: Treatise on Geochemistry: Oxford, 1–39, Elsevier, http://dx.doi.org/10.1016/B978-0-08-095975-7.00201-1, 2014.

Rotenberg, E., Davis, D. W., Amelin, Y., Ghosh, S., and Bergquist, B. A.: Determination of the decay-constant of ^{87}Rb by laboratory accumulation of ^{87}Sr, Geochimica et Cosmochimica Acta, 85, 41–57, https://doi.org/10.1016/j.gca.2012.01.016, 2012.

Smithies, R. H., Van Kranendonk, M. J., and Champion, D. C.: It started with a plume–early Archaean basaltic proto-continental crust, Earth and Planetary Science Letters, 238, 284–297, https://doi.org/10.1016/j.epsl.2005.07.023, 2005.

Tusch, J., Münker, C., Hasenstab, E., Jansen, M., Marien, C. S., Kurzweil, F., Van Kranendonk, M. J., Smithies, H., Maier, W., and Garbe- Schönberg, D.: Convective isolation of Hadean mantle reservoirs through Archean time, Proceedings of the National Academy of Sciences, 118, e2012626 118, https://doi.org/10.1073/pnas.2012626118, 2021.

Van Kranendonk, M. J., Hickman, A. H., Smithies, R. H., Nelson, D. R., and Pike, G.: Geology and tectonic evolution of the Archean North Pilbara terrain, Pilbara Craton, Western Australia, Economic Geology, 97, 695–732, https://doi.org/10.2113/gsecongeo.97.4.695, 2002.

Van Kranendonk, M. J., Smithies, R. H., Hickman, A. H., and Champion, D. C.: Paleoarchean development of a continental nucleus: the East Pilbara terrane of the Pilbara craton, Western Australia, Developments in Precambrian geology, 15, 307–337, https://doi.org/10.1016/S0166-2635(07)15041-6, 2007.

Van Kranendonk, M. J., Smithies, R. H., Griffin, W. L., Huston, D. L., Hickman, A. H., Champion, D. C., Anhaeusser, C. R., and Pirajno, F.: Making it thick: a volcanic plateau origin of Palaeoarchean continental lithosphere of the Pilbara and Kaapvaal cratons, Geological Society, London, Special Publications, 389, 83–111, https://doi.org/10.1144/SP389.12, 2015.

Van Kranendonk, M. J., Smithies, R. H., Hickman, A. H., and Champion, D. C.: Paleoarchean development of a continental nucleus: the East Pilbara Terrane of the Pilbara Craton, Western Australia, in: Earth's Oldest Rocks, edited by Van Kranendonk, M., Bennett, V., and Hoffmann, J., 437 – 462, Elsevier, https://doi.org/10.1016/B978-0-444-63901-1.00019-8, 2019.

Vermeesch, P.: IsoplotR: a free and open toolbox for geochronology, Geoscience Frontiers, 9, 1479-1493, https://doi.org/10.1016/j.gsf.2018.04.001, 2018.

Willbold, M. and Jochum, K. P.: Multi-element isotope dilution sector field ICP-MS: A precise technique for the analysis of geological materials and its application to geological reference materials, Geostandards and Geoanalytical Research, 29, 63–82, https://doi.org/10.1111/j.1751-908X.2005.tb00656.x, 2005.

Xiang, W.: Carbonate factories in the early Archean and their geobiological impacts, Ph.D. thesis, University of Göttingen, Germany, http://dx.doi.org/10.53846/goediss-10047, 2023.